

# Supplementary Material:

## Modeling Temporal Coherence for Optical Flow

13th International Conference on Computer Vision  
Nov. 2011, Barcelona, Spain

## 1 Linearization and Normalization

As mentioned in the main paper, we follow a coarse-to-fine multi-scale approach similar to [7] and approximate the original nonconvex model by a series of convex energies defined on different resolution levels. Assuming that the four flows  $\vec{w}_i$  are available from a coarser scale, the goal on each resolution level is then to express the total energy in terms of the flow increments  $d\vec{w}_i = (du_i, dv_i)^\top$  with  $i = 1, \dots, 4$ . Similar to [9] this allows us to introduce a tensor notation which makes the convexity of the resulting energy functional explicit and which enables us to apply a normalization strategy that makes deviations from the model assumptions interpretable in a geometric way.

### 1.1 Linearization in the Data Term

Let us first illustrate the incremental formulation of the data term by the example of the simplified data constraint

$$\mathcal{E}_{d12} = \theta \cdot \Psi_d (|g_2(\vec{x} - \vec{w}_2) - g_1(\vec{x} - \vec{w}_2 - \vec{w}_1)|^2) , \quad (1)$$

which we rewrite using the flow increments as

$$\mathcal{E}_{d12} = \theta \cdot \Psi_d (|g_2(\vec{x} - \vec{w}_2 - d\vec{w}_2) - g_1(\vec{x} - \vec{w}_2 - d\vec{w}_2 - \vec{w}_1 - d\vec{w}_1)|^2) . \quad (2)$$

In a first step, we perform a first order Taylor expansion to linearize the constraint in the above data term w.r.t. all flow increments. In this way we obtain the approximation

$$\begin{aligned} & g_2(\vec{x} - \vec{w}_2 - d\vec{w}_2) - g_1(\vec{x} - \vec{w}_2 - d\vec{w}_2 - \vec{w}_1 - d\vec{w}_1) \\ & \approx g_2 - \partial_x g_2 \cdot (du_2) - \partial_y g_2 \cdot (dv_2) \\ & \quad - g_1 + \partial_x g_1 \cdot (du_2 + du_1) + \partial_y g_1 \cdot (dv_2 + dv_1) . \end{aligned} \quad (3)$$

Rearranging the terms using the following abbreviations

$$g_{1x} = \partial_x g_1(\vec{x} - \vec{w}_2 - \vec{w}_1) , \quad (4)$$

$$g_{1y} = \partial_y g_1(\vec{x} - \vec{w}_2 - \vec{w}_1) , \quad (5)$$

$$g_{1z} = g_2(\vec{x} - \vec{w}_2) - g_1(\vec{x} - \vec{w}_2 - \vec{w}_1) , \quad (6)$$

$$g_{1xz} = \partial_x g_{1z} , \quad g_{1yz} = \partial_y g_{1z} , \quad (7)$$

we can rewrite the linearized constraint (3) as the inner product

$$\vec{g}_{12}^\top \vec{d} = g_{1x}du_1 + g_{1y}dv_1 - g_{1xz}du_2 - g_{1yz}dv_2 + g_{1z} , \quad (8)$$

with the two vectors  $\vec{g}_{12}$  and  $\vec{d}$  being defined as

$$\vec{g}_{12} = (g_{1x}, g_{1y}, -g_{1xz}, -g_{1yz}, 0, 0, 0, 0, g_{1z})^\top , \quad (9)$$

$$\vec{d} = (du_1, dv_1, du_2, dv_2, du_3, dv_3, du_4, dv_4, 1)^\top . \quad (10)$$

As in [9], such a product can be seen as a multidimensional extension of the classical optical flow constraint [6]. Inserting it as squared argument into the penalizer  $\Psi$  yields the robustified quadratic form

$$\mathcal{E}_{d12} = \Psi_d \left( (\vec{g}_{12}^\top \vec{d})^2 \right) = \Psi_d \left( \vec{d}^\top J_{12} \vec{d} \right) , \quad (11)$$

where  $J_{12} = \vec{g}_{12} \vec{g}_{12}^\top$  is a  $9 \times 9$  matrix that provides coupling between the increments of the first two flows. By analogy to the motion tensor notation in optical flow estimation [3], we denote  $J_{12}$  as *trajectorial motion tensor*. The linearization of the three remaining data constraints is carried out accordingly and results in the  $9 \times 9$  trajectorial motion tensors  $J_{23}$ ,  $J_{34}$  and  $J_{45}$ . Missing dependencies between the variables will give rise to zero tensor entries. Including the gradient constancy assumption and extending it to RGB color images as in equation (7) in the paper is straightforward and leads to a weighted sum of the corresponding tensors [10].

## 1.2 Constraint Normalization

In [10] the authors demonstrate that the linearized brightness constancy assumption for optical flow can be interpreted geometrically as a weighted distance of the estimated flow to the line described by the optical flow constraint. To compensate for this weighting they propose a normalization of the data constraints such that deviations can be interpreted as actual geometric distances in the space of unknowns. This idea was generalized in [9] to the multidimensional case in the context of scene flow estimation. Thereby it was shown that if the constraints are formulated as quadratic forms, this strategy yields a normalization of the corresponding tensor entries by the *reduced trace*. For our previous example of the data term  $\mathcal{E}_{d12}$  with the constraint being defined by the hyperplane  $\vec{g}_{12}^\top \vec{d} = 0$ , such a normalization gives

$$\frac{(\vec{g}_{12}^\top \vec{d})^2}{|\vec{n}|^2 + \zeta^2} = \vec{d}^\top \underbrace{\left( \frac{J_{12}}{\sum_{i=1}^8 (J_{12})_{ii} + \zeta^2} \right)}_{\text{reduced trace}} \vec{d} = \vec{d}^\top \hat{J}_{12} \vec{d} , \quad (12)$$

where  $\vec{n} = (g_{1x}, g_{1y}, -g_{1xz}, -g_{1yz}, 0, 0, 0, 0, 0)^\top$  is the hyperplane normal,  $\zeta = 0.1$  is a small constant that avoids division by zero and  $\hat{J}_{12}$  is the normalized version of  $J_{12}$ . We apply the same normalization strategy to the remaining data constraints and in accordance to [10] also to the different components of the regularization tensor  $R_\rho$  from which we compute the local constraint directions  $\vec{r}_1$  and  $\vec{r}_2$ . We further refer to [10] for the extension of the normalization to the gradient constancy assumption and color images.

## 2 Incremental Energy

After we have discussed the linearization and the normalization of the data constraints, we can finally write down the incremental energy that has to be minimized on each resolution level of the coarse-to-fine multi-resolution scheme in order to determine the four flow increments  $\vec{w}_i$ , i.e. the eight variables  $du_1, dv_1, du_2, dv_2, du_3, dv_3, du_4, dv_4$ . In our case, this energy is given by

$$\mathcal{E}(du_1, dv_1, du_2, dv_2, du_3, dv_3, du_4, dv_4) = \quad (13)$$

$$\begin{aligned}
& \int_{\Omega} \left[ \theta \Psi_d \left( \vec{d}^\top \widehat{J}_{1|12} \vec{d} \right) + \Psi_d \left( \vec{d}^\top \widehat{J}_{1|23} \vec{d} \right) + \Psi_d \left( \vec{d}^\top \widehat{J}_{1|34} \vec{d} \right) + \theta \Psi_d \left( \vec{d}^\top \widehat{J}_{1|45} \vec{d} \right) \right] d\vec{x} \\
& + \int_{\Omega} \left[ \theta \Psi_d \left( \vec{d}^\top \widehat{J}_{2|12} \vec{d} \right) + \Psi_d \left( \vec{d}^\top \widehat{J}_{2|23} \vec{d} \right) + \Psi_d \left( \vec{d}^\top \widehat{J}_{2|34} \vec{d} \right) + \theta \Psi_d \left( \vec{d}^\top \widehat{J}_{2|45} \vec{d} \right) \right] d\vec{x} \\
& + \alpha \int_{\Omega} \left[ \Psi_{s_1} \left( \sum_{i=1}^4 \nu_i \left( (\vec{r}_1^\top \nabla(u_i + du_i))^2 + (\vec{r}_1^\top \nabla(v_i + dv_i))^2 \right) \right) \right] d\vec{x} \\
& + \alpha \int_{\Omega} \left[ \Psi_{s_2} \left( \sum_{i=1}^4 \nu_i \left( (\vec{r}_2^\top \nabla(u_i + du_i))^2 + (\vec{r}_2^\top \nabla(v_i + dv_i))^2 \right) \right) \right] d\vec{x} \\
& + \beta_1 \int_{\Omega} \left[ \sum_{i=1}^3 \Psi_t \left( ((u_{i+1} + du_{i+1}) - (u_i + du_i))^2 + ((v_{i+1} + dv_{i+1}) - (v_i + dv_i))^2 \right) \right] d\vec{x} \\
& + \beta_2 \int_{\Omega} \left[ \sum_{i=2}^3 \Psi_t \left( \begin{aligned} & \left( (u_{i+1} + du_{i+1}) - 2(u_i + du_i) + (u_{i-1} + du_{i-1}) \right)^2 \\ & + \left( (v_{i+1} + dv_{i+1}) - 2(v_i + dv_i) + (v_{i-1} + dv_{i-1}) \right)^2 \end{aligned} \right) \right] d\vec{x} .
\end{aligned}$$

### 3 Minimization

In order to minimize the incremental energy in (13) we have to solve the associated Euler-Lagrange equations. Here, we exploit the relation between the weights  $\nu_i$  of the smoothness term and the weight  $\theta$  of the data term that is given in Sec. 2.4 of the main paper:  $\nu_1 = \nu_4 = \theta$  and  $\nu_2 = \nu_3 = 1 + \theta$ . In this way we obtain the following system of eight coupled partial differential equations:

$$\begin{aligned}
0 = & \theta \cdot \Psi'_{d1|12} \cdot \left( \widehat{J}_{1|12|11} du_1 + \widehat{J}_{1|12|12} dv_1 + \widehat{J}_{1|12|13} du_2 + \widehat{J}_{1|12|14} dv_2 + \widehat{J}_{1|12|19} \right) \quad (14) \\
& + \theta \cdot \Psi'_{d2|12} \cdot \left( \widehat{J}_{2|12|11} du_1 + \widehat{J}_{2|12|12} dv_1 + \widehat{J}_{2|12|13} du_2 + \widehat{J}_{2|12|14} dv_2 + \widehat{J}_{2|12|19} \right) \\
& - \alpha (\theta) \operatorname{div} \left( D \cdot \nabla(u_1 + du_1) \right) \\
& + \beta_1 \cdot \Psi'_{t11} \cdot \left( (u_1 + du_1) - (u_2 + du_2) \right) \\
& + \beta_2 \cdot \Psi'_{t22} \cdot \left( (u_3 + du_3) - 2(u_2 + du_2) + (u_1 + du_1) \right)
\end{aligned}$$

$$\begin{aligned}
0 = & \theta \cdot \Psi'_{d1|12} \cdot \left( \widehat{J}_{1|12|21} du_1 + \widehat{J}_{1|12|22} dv_1 + \widehat{J}_{1|12|23} du_2 + \widehat{J}_{1|12|24} dv_2 + \widehat{J}_{1|12|29} \right) \quad (15) \\
& + \theta \cdot \Psi'_{d2|12} \cdot \left( \widehat{J}_{2|12|21} du_1 + \widehat{J}_{2|12|22} dv_1 + \widehat{J}_{2|12|23} du_2 + \widehat{J}_{2|12|24} dv_2 + \widehat{J}_{2|12|29} \right) \\
& -\alpha (\theta) \operatorname{div} \left( D \cdot \nabla (v_1 + dv_1) \right) \\
& + \beta_1 \cdot \Psi'_{t11} \cdot \left( (v_1 + dv_1) - (v_2 + dv_2) \right) \\
& + \beta_2 \cdot \Psi'_{t22} \cdot \left( (v_3 + dv_3) - 2(v_2 + dv_2) + (v_1 + dv_1) \right)
\end{aligned}$$

$$\begin{aligned}
0 = & \theta \cdot \Psi'_{d1|12} \cdot \left( \widehat{J}_{1|12|31} du_1 + \widehat{J}_{1|12|32} dv_1 + \widehat{J}_{1|12|33} du_2 + \widehat{J}_{1|12|34} dv_2 + \widehat{J}_{1|12|39} \right) \quad (16) \\
& + \theta \cdot \Psi'_{d2|12} \cdot \left( \widehat{J}_{2|12|31} du_1 + \widehat{J}_{2|12|32} dv_1 + \widehat{J}_{2|12|33} du_2 + \widehat{J}_{2|12|34} dv_2 + \widehat{J}_{2|12|39} \right) \\
& + 1 \cdot \Psi'_{d1|23} \cdot \left( \widehat{J}_{1|23|33} du_2 + \widehat{J}_{1|23|34} dv_2 + \widehat{J}_{1|23|39} \right) \\
& + 1 \cdot \Psi'_{d2|23} \cdot \left( \widehat{J}_{2|23|33} du_2 + \widehat{J}_{2|23|34} dv_2 + \widehat{J}_{2|23|39} \right) \\
& -\alpha (1 + \theta) \operatorname{div} \left( D \cdot \nabla (u_2 + du_2) \right) \\
& + \beta_1 \cdot \Psi'_{t11} \cdot \left( (u_2 + du_2) - (u_1 + du_1) \right) \\
& + \beta_1 \cdot \Psi'_{t12} \cdot \left( (u_2 + du_2) - (u_3 + du_3) \right) \\
& + \beta_2 \cdot \Psi'_{t22} \cdot \left( (u_3 + du_3) - 2(u_2 + du_2) + (u_1 + du_1) \right) \cdot (-2) \\
& + \beta_2 \cdot \Psi'_{t23} \cdot \left( (u_4 + du_4) - 2(u_3 + du_3) + (u_2 + du_2) \right)
\end{aligned}$$

$$\begin{aligned}
0 = & \theta \cdot \Psi'_{d1|12} \cdot \left( \widehat{J}_{1|12|41} du_1 + \widehat{J}_{1|12|42} dv_1 + \widehat{J}_{1|12|43} du_2 + \widehat{J}_{1|12|44} dv_2 + \widehat{J}_{1|12|49} \right) \quad (17) \\
& + \theta \cdot \Psi'_{d2|12} \cdot \left( \widehat{J}_{2|12|41} du_1 + \widehat{J}_{2|12|42} dv_1 + \widehat{J}_{2|12|43} du_2 + \widehat{J}_{2|12|44} dv_2 + \widehat{J}_{2|12|49} \right) \\
& + 1 \cdot \Psi'_{d1|23} \cdot \left( \widehat{J}_{1|23|43} du_2 + \widehat{J}_{1|23|44} dv_2 + \widehat{J}_{1|23|49} \right) \\
& + 1 \cdot \Psi'_{d2|23} \cdot \left( \widehat{J}_{2|23|43} du_2 + \widehat{J}_{2|23|44} dv_2 + \widehat{J}_{2|23|49} \right) \\
& -\alpha (1 + \theta) \operatorname{div} \left( D \cdot \nabla (v_2 + dv_2) \right) \\
& + \beta_1 \cdot \Psi'_{t11} \cdot \left( (v_2 + dv_2) - (v_1 + dv_1) \right) \\
& + \beta_1 \cdot \Psi'_{t12} \cdot \left( (v_2 + dv_2) - (v_3 + dv_3) \right) \\
& + \beta_2 \cdot \Psi'_{t22} \cdot \left( (v_3 + dv_3) - 2(v_2 + dv_2) + (v_1 + dv_1) \right) \cdot (-2) \\
& + \beta_2 \cdot \Psi'_{t23} \cdot \left( (v_4 + dv_4) - 2(v_3 + dv_3) + (v_2 + dv_2) \right)
\end{aligned}$$

$$\begin{aligned}
0 = & 1 \cdot \Psi'_{d1|34} \cdot \left( \widehat{J}_{1|34|55} du_3 + \widehat{J}_{1|34|56} dv_3 \right. \\
& \left. + \widehat{J}_{1|34|59} \right) \quad (18) \\
& + 1 \cdot \Psi'_{d2|34} \cdot \left( \widehat{J}_{2|34|55} du_3 + \widehat{J}_{2|34|56} dv_3 \right. \\
& \left. + \widehat{J}_{2|34|59} \right) \\
& + \theta \cdot \Psi'_{d1|45} \cdot \left( \widehat{J}_{1|45|55} du_3 + \widehat{J}_{1|45|56} dv_3 + \widehat{J}_{1|45|57} du_4 + \widehat{J}_{1|45|58} dv_4 + \widehat{J}_{1|45|59} \right) \\
& + \theta \cdot \Psi'_{d2|45} \cdot \left( \widehat{J}_{2|45|55} du_3 + \widehat{J}_{2|45|56} dv_3 + \widehat{J}_{2|45|57} du_4 + \widehat{J}_{2|45|58} dv_4 + \widehat{J}_{2|45|59} \right) \\
& - \alpha (1 + \theta) \operatorname{div} \left( D \cdot \nabla (u_3 + du_3) \right) \\
& + \beta_1 \cdot \Psi'_{t12} \cdot \left( (u_3 + du_3) - (u_2 + du_2) \right) \\
& + \beta_1 \cdot \Psi'_{t13} \cdot \left( (u_3 + du_3) - (u_4 + du_4) \right) \\
& + \beta_2 \cdot \Psi'_{t22} \cdot \left( (u_3 + du_3) - 2(u_2 + du_2) + (u_1 + du_1) \right) \\
& + \beta_2 \cdot \Psi'_{t23} \cdot \left( (u_4 + du_4) - 2(u_3 + du_3) + (u_2 + du_2) \right) \cdot (-2)
\end{aligned}$$

$$\begin{aligned}
0 = & 1 \cdot \Psi'_{d1|34} \cdot \left( \widehat{J}_{1|34|65} du_3 + \widehat{J}_{1|34|66} dv_3 \right. \\
& \left. + \widehat{J}_{1|34|69} \right) \quad (19) \\
& + 1 \cdot \Psi'_{d2|34} \cdot \left( \widehat{J}_{2|34|65} du_3 + \widehat{J}_{2|34|66} dv_3 \right. \\
& \left. + \widehat{J}_{2|34|69} \right) \\
& + \theta \cdot \Psi'_{d1|45} \cdot \left( \widehat{J}_{1|45|65} du_3 + \widehat{J}_{1|45|66} dv_3 + \widehat{J}_{1|45|67} du_4 + \widehat{J}_{1|45|68} dv_4 + \widehat{J}_{1|45|69} \right) \\
& + \theta \cdot \Psi'_{d2|45} \cdot \left( \widehat{J}_{2|45|65} du_3 + \widehat{J}_{2|45|66} dv_3 + \widehat{J}_{2|45|67} du_4 + \widehat{J}_{2|45|68} dv_4 + \widehat{J}_{2|45|69} \right) \\
& - \alpha (1 + \theta) \operatorname{div} \left( D \cdot \nabla (v_3 + dv_3) \right) \\
& + \beta_1 \cdot \Psi'_{t12} \cdot \left( (v_3 + dv_3) - (v_2 + dv_2) \right) \\
& + \beta_1 \cdot \Psi'_{t13} \cdot \left( (v_3 + dv_3) - (v_4 + dv_4) \right) \\
& + \beta_2 \cdot \Psi'_{t22} \cdot \left( (v_3 + dv_3) - 2(v_2 + dv_2) + (v_1 + dv_1) \right) \\
& + \beta_2 \cdot \Psi'_{t23} \cdot \left( (v_4 + dv_4) - 2(v_3 + dv_3) + (v_2 + dv_2) \right) \cdot (-2)
\end{aligned}$$

$$\begin{aligned}
0 = & \theta \cdot \Psi'_{d1|45} \cdot \left( \widehat{J}_{1|45|75} du_3 + \widehat{J}_{1|45|76} dv_3 + \widehat{J}_{1|45|77} du_4 + \widehat{J}_{1|45|78} dv_4 + \widehat{J}_{1|45|79} \right) \quad (20) \\
& + \theta \cdot \Psi'_{d2|45} \cdot \left( \widehat{J}_{2|45|75} du_3 + \widehat{J}_{2|45|76} dv_3 + \widehat{J}_{2|45|77} du_4 + \widehat{J}_{2|45|78} dv_4 + \widehat{J}_{2|45|79} \right) \\
& - \alpha (\theta) \operatorname{div} \left( D \cdot \nabla (u_4 + du_4) \right) \\
& + \beta_1 \cdot \Psi'_{t13} \cdot \left( (u_4 + du_4) - (u_3 + du_3) \right) \\
& + \beta_2 \cdot \Psi'_{t23} \cdot \left( (u_4 + du_4) - 2(u_3 + du_3) + (u_2 + du_2) \right)
\end{aligned}$$

$$\begin{aligned}
0 = & \theta \cdot \Psi'_{d1|45} \cdot \left( \widehat{J}_{1|45|85} du_3 + \widehat{J}_{1|45|86} dv_3 + \widehat{J}_{1|45|87} du_4 + \widehat{J}_{1|45|88} dv_4 + \widehat{J}_{1|45|89} \right) \quad (21) \\
& + \theta \cdot \Psi'_{d2|45} \cdot \left( \widehat{J}_{2|45|85} du_3 + \widehat{J}_{2|45|86} dv_3 + \widehat{J}_{2|45|87} du_4 + \widehat{J}_{2|45|88} dv_4 + \widehat{J}_{2|45|89} \right) \\
& - \alpha (\theta) \operatorname{div} \left( D \cdot \nabla (v_4 + dv_4) \right) \\
& + \beta_1 \cdot \Psi'_{t13} \cdot \left( (v_4 + dv_4) - (v_3 + dv_3) \right) \\
& + \beta_2 \cdot \Psi'_{t23} \cdot \left( (v_4 + dv_4) - 2(v_3 + dv_3) + (v_2 + dv_2) \right)
\end{aligned}$$

where  $\widehat{J}_{kl|mn}$  denotes the entry in row  $m$  and column  $n$  of the trajectory motion tensor  $\widehat{J}_{kl}$ . Further note that zero-entries in the trajectory motion tensors are omitted in the above Euler-Lagrange equations to keep notation as short as possible.

Due to the particular choice of the spatial smoothness weights  $\nu_i$  in the energy (13), the contributions of the data terms and the spatial smoothness terms are now in balance for each of the resulting eight PDEs (14)-(21). In this context, also the desired emphasis on the inner data terms becomes explicit: Since we have chosen  $\theta = 0.5$ , the inner data terms  $\mathcal{E}_{23}$  and  $\mathcal{E}_{34}$  contribute twice as much to the inner flow fields  $\vec{w}_2, \vec{w}_3$  than the outer data terms  $\mathcal{E}_{12}$  and  $\mathcal{E}_{45}$ . Moreover, the two smoothness terms of the joint spatial regularization result in a continuous 2-D nonlinear anisotropic diffusion process of second order in the image plane (see [10]). On the other hand, the contributions of the discrete trajectory smoothness assumptions to the Euler-Lagrange equations can be interpreted as discrete 1-D nonlinear diffusion process of second and fourth order in trajectory direction, respectively. Thereby, the spatial anisotropic diffusion process induced by the joint spatial regularization is steered by a *joint* nonlinear diffusion tensor  $D$  for all flows which reads

$$D := \Psi'_{s_1} \cdot \vec{r}_1 \vec{r}_1^\top + \Psi'_{s_2} \cdot \vec{r}_2 \vec{r}_2^\top, \quad (22)$$

where

$$\Psi'_{s_1} := \Psi'_{s_1} \left( \sum_{i=1}^4 \nu_i \left( (\vec{r}_1^\top \nabla (u_i + du_i))^2 + (\vec{r}_1^\top \nabla (v_i + dv_i))^2 \right) \right) \quad (23)$$

$$\Psi'_{s_2} := \Psi'_{s_2} \left( \sum_{i=1}^4 \nu_i \left( (\vec{r}_2^\top \nabla (u_i + du_i))^2 + (\vec{r}_2^\top \nabla (v_i + dv_i))^2 \right) \right) \quad (24)$$

The remaining nonlinear expressions from the data term and the trajectory terms read

$$\Psi'_{di|kl} := \Psi'_{di} \left( \vec{d}^\top \widehat{J}_{i|kl} \vec{d} \right), \quad (25)$$

$$\Psi'_{t1i} := \Psi'_t \left( \left( (u_{i+1} + du_{i+1}) - (u_i + du_i) \right)^2 + \left( (v_{i+1} + dv_{i+1}) - (v_i + dv_i) \right)^2 \right) \quad (26)$$

$$\begin{aligned}
\Psi'_{t2i} := & \Psi'_t \left( \left( (u_{i+1} + du_{i+1}) - 2(u_i + du_i) + (u_{i-1} + du_{i-1}) \right)^2 \right. \\
& \left. + \left( (v_{i+1} + dv_{i+1}) - 2(v_i + dv_i) + (v_{i-1} + dv_{i-1}) \right)^2 \right),
\end{aligned} \quad (27)$$

The derivatives of all nonlinear functions with respect to the squared argument are furthermore

given by

$$\Psi'_{di}(s^2) = \frac{1}{2\sqrt{s^2 + \varepsilon^2}} \quad (28)$$

$$\Psi'_{s_1}(s^2) = \frac{1}{1 + \frac{s^2}{\lambda_1^2}} \quad (29)$$

$$\Psi'_{s_2}(s^2) = \frac{1}{\sqrt{1 + \frac{s^2}{\lambda_2^2}}} \quad (30)$$

$$\Psi'_{t}(s^2) = \frac{1}{\sqrt{1 + \frac{s^2}{\lambda_3^2}}} \quad (31)$$

## 4 Solution of the Nonlinear System

After spatially discretizing the time-discrete Euler-Lagrange equations via finite differences, we obtain a large sparse nonlinear system of equations with  $8N_l$  unknowns for each level  $l$ , where  $N_l$  is the number of pixels. This system is then solved based on the highly efficient bidirectional nonlinear multigrid scheme from [4] – a so called full approximation scheme (FAS) [2]. To speed up the exchange of information between the unknowns, a nonlinear point-coupled  $8 \times 8$  Gauß-Seidel method [3] based on frozen coefficients [5] is used as basis solver. This method computes the solution for all eight unknowns of each pixel simultaneously such that we do not have to alternate between the different flows in the optimization. Moreover, it is straightforward to extend the proof in [8] such that it is possible to show that the system matrices for frozen (fixed) nonlinear coefficients are positive semi-definite. In fact, for non-degenerated cases, i.e. images sequences with at least two independent non-vanishing gradients per image, the system matrices are even positive definite. Apart from ensuring a unique solution on each resolution level, this guarantees convergence of our basis solver. The different components of the full multigrid scheme were chosen in accordance with [3].

## 5 Baseline Method with Trajectoral Stabilization

In our first experiment presented in Sec. 5 we compare the proposed temporal coherent (TC) optical flow method against (i) the baseline method with *purely spatial* regularization (Complementary Optic Flow [10]), (ii) the baseline method with *spatio-temporal* regularization (also proposed in [10]) and (iii) a variant of the baseline method with *trajectorial stabilization* (following [1] but with stabilization both forward and backward in time).

As there is no paper that exactly describes the method in (iii), we briefly sketch the underlying ideas in the following. In order to add a trajectorial stabilization to the baseline method [10], we extend the original energy by a third term  $\mathcal{E}_{stab}$ , resulting in

$$\mathcal{E} = \int_{\Omega} (\mathcal{E}_d^{\text{COF}} + \mathcal{E}_s^{\text{COF}} + \mathcal{E}_{stab}) \, d\vec{x} , \quad (32)$$

where  $\mathcal{E}_d^{\text{COF}}$  and  $\mathcal{E}_s^{\text{COF}}$  denote the data term and the smoothness term of the baseline method, respectively. The stabilization term is given by

$$\mathcal{E}_{stab} = \beta \left( \Psi_{stab}(|\vec{w} - \vec{w}_-|^2) + \Psi_{stab}(|\vec{w} - \vec{w}_+|^2) \right) , \quad (33)$$

with a weight  $\beta > 0$  that balances the stabilization term against the two other terms. Here, the two flow fields  $\vec{w}_-$  and  $\vec{w}_+$  are the flows between the previous and the next image pair of the sequence, however registered to the central frame. The registration is achieved by warping the flow fields by their own motion. Also note that the two flows are precomputed using the baseline method. As proposed in [1], we use a subquadratic penalizer function that in our case is given by the regularized  $L_1$  norm  $\Psi_{stab}(s^2) = \sqrt{s^2 + \varepsilon^2}$ .

Two problems that may arise when warping the flow fields are: (i) There will be no flow vector at occlusions, and (ii) more than one flow vector is generated at disocclusions. We thus disable the stabilization at those problematic locations that can be identified during the warping procedure itself. This is realized by multiplying the two summands of the stabilization term by binary weights  $c_-$  and  $c_+$  that are equal to zero at occlusions and disocclusions, and equal to one elsewhere.

## 6 Additional Results for the Middlebury Datasets

In the following Fig. 1–2 we show results on the Middlebury training data set as well as on the evaluation data set. In particular, we give the four flow fields along the motion trajectory  $\vec{w}_1$  to  $\vec{w}_4$  and additionally the computed trajectorial model map. If we consider the four flows for Army, Grove and Urban in Fig. 2 we see that the motion rapidly changes over time: While the cloth in the background of the Army sequence moves abruptly in the fourth flow, the branches in the Grove sequence move faster in the first two flows. In the Urban sequence, due to a combined translation and rotation of the camera, the relative motion decreases over time. Furthermore, one also verifies that the trajectorial model maps make sense. Particularly good results can be obtained at the Hydrangea, Grove 2 and Wooden sequence. The other maps are still reasonable, but a bit more noisy.

All flow fields are best viewed in the electronic PDF version.

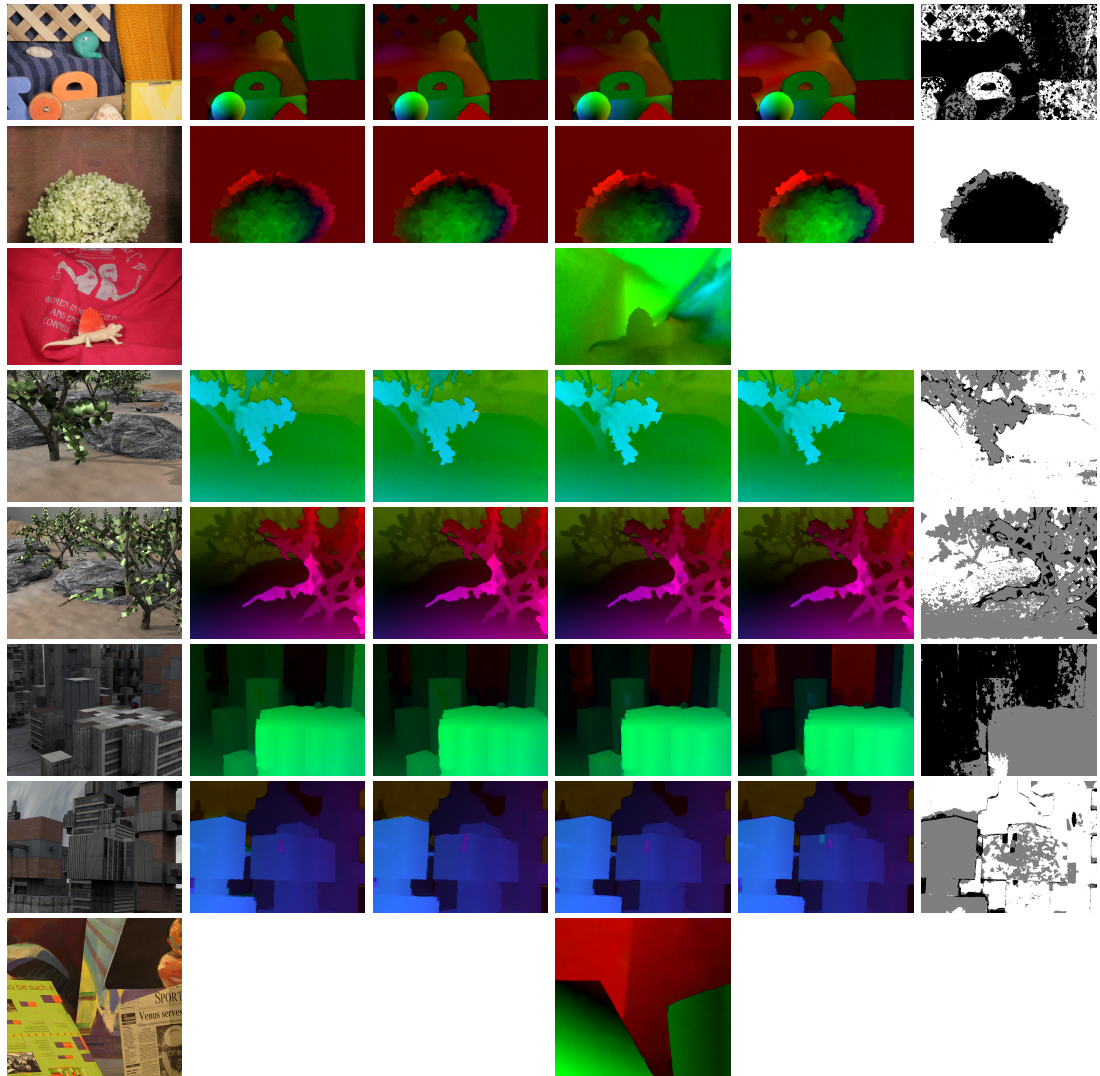


Figure 1: Results on the Middlebury training data set. **Left to right:** Reference frame, Flows  $\vec{w}_1$  to  $\vec{w}_4$  without trajectorial regularization (TC joint spatial), computed trajectorial model map (black: none, gray: 2nd order, white: 1st order). **Top to bottom:** RubberWhale, Hydrangea, Dimetrodon, Grove 2, Grove 3, Urban 2, Urban 3, Venus.

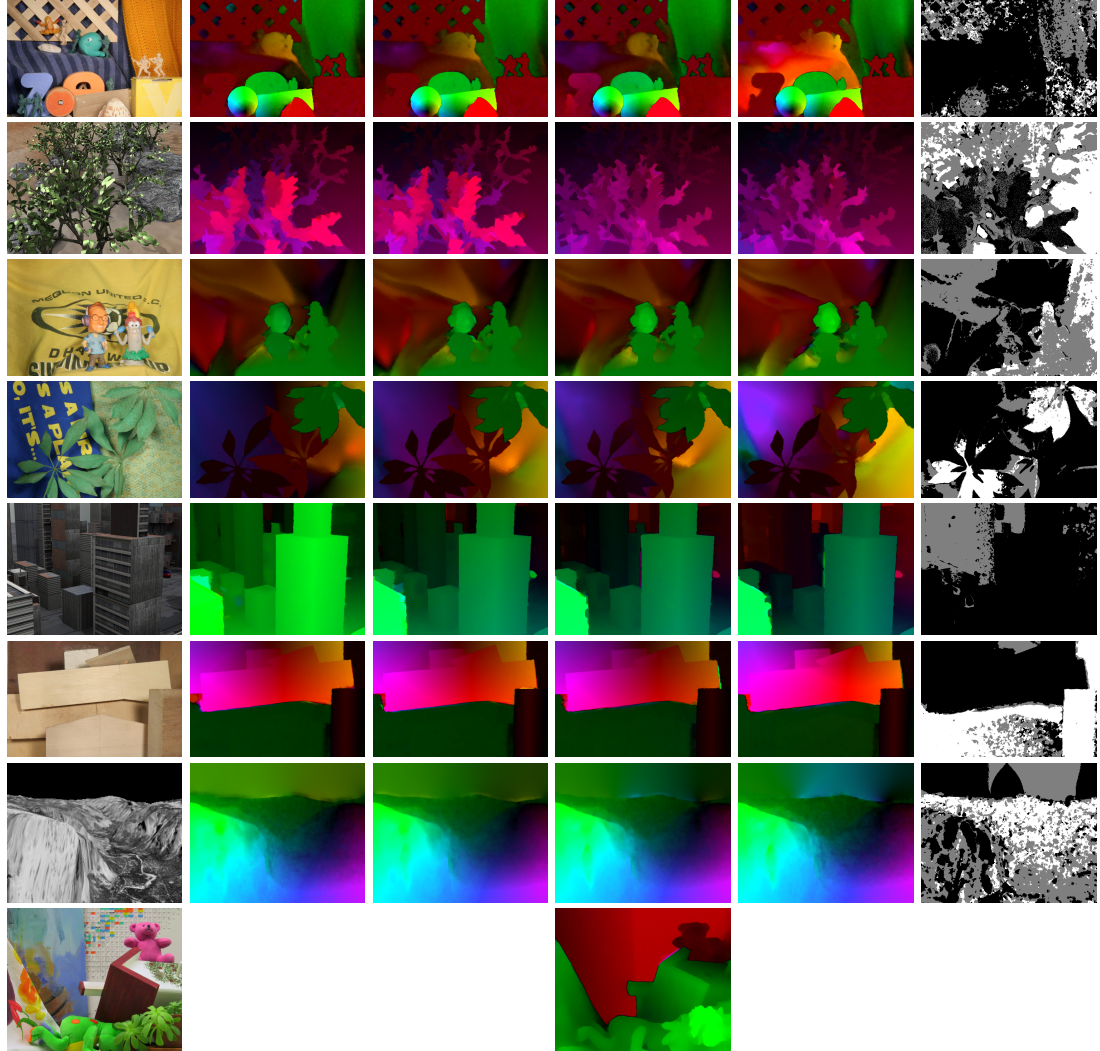


Figure 2: Results on the Middlebury evaluation data set. **Left to right:** Reference frame, Flows  $\bar{w}_1$  to  $\bar{w}_4$  without trajectory regularization (TC joint spatial), computed trajectory model map (black: none, gray: 2nd order, white: 1st order). **Top to bottom:** Army, Grove, Mequon, Schefflera, Urban, Wooden, Yosemite, Teddy.

## 7 Results on a Real-World Traffic Sequence

To show the benefits of a trajectorial regularizer we compare the baseline method with purely spatial regularization [10] to our method with a second order trajectorial regularization on a real-world traffic sequence<sup>1</sup>. A corresponding video is also part of the supplementary material. Below, we show two exemplary screenshots of this video. As one can see in Fig. 3, the background noise is significantly reduced when using a trajectorial regularizer. Furthermore, the motion boundaries of the cars are much sharper due to the joint spatial regularizer that enforces coherent flow structures along trajectories. While our first observation is a new insight of this experiment, the latter is in accordance with our findings from Fig. 3 in the paper. In the second screenshot that is shown in Fig. 4 another advantage of the trajectorial regularizer is illustrated: Estimating the motion of partly occluded objects such as the car marked with the white circle becomes possible.

All flow fields are best viewed in the electronic PDF version.

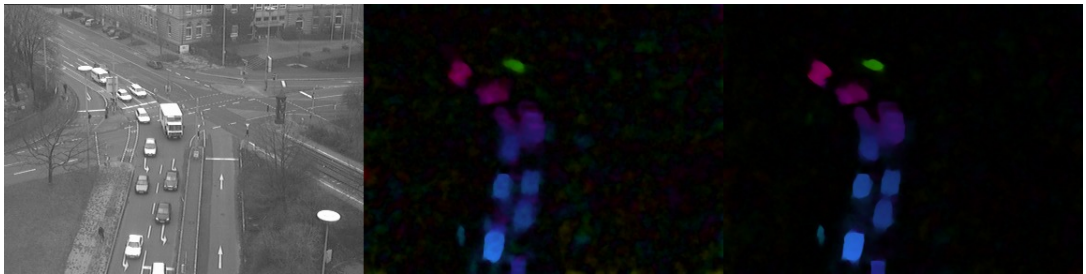


Figure 3: **Left:** Reference frame. **Middle:** Flow field of the baseline method [10] with a purely spatial regulariser. **Right:** Our result with second order trajectorial regularization. Note that the noise in the background is reduced and also the motion boundaries of the cars are much sharper.

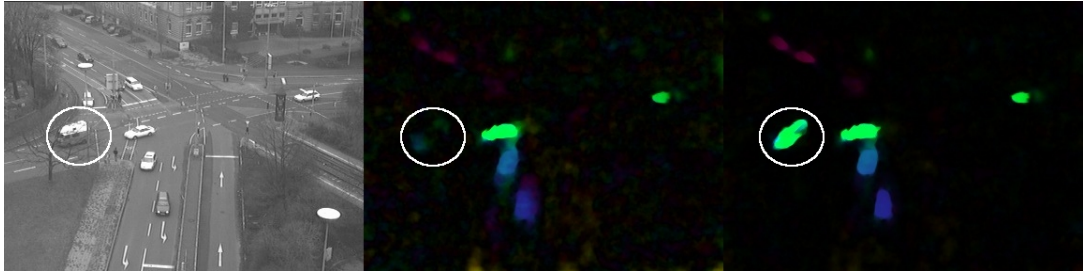


Figure 4: **Left:** Reference frame. **Middle:** Flow field of the baseline method [10] with a purely spatial regulariser. **Right:** Our result with second order trajectorial regularization. Note that the motion of the car in the white circle is still reasonably estimated, while it is not even present in the middle flow field.

<sup>1</sup>dt\_passat, available at [http://i21www.ira.uka.de/image\\_sequences/](http://i21www.ira.uka.de/image_sequences/)

## References

- [1] M. J. Black and P. Anandan. Robust dynamic motion estimation over time. In *Proc. 1991 IEEE Computer Society Conference on Computer Vision and Pattern Recognition*, pages 292–302, Maui, HI, June 1991. IEEE Computer Society Press.
- [2] A. Brandt. Multi-level adaptive solutions to boundary-value problems. *Mathematics of Computation*, 31(138):333–390, April 1977.
- [3] A. Bruhn and J. Weickert. Towards ultimate motion estimation: Combining highest accuracy with real-time performance. In *Proc. Tenth International Conference on Computer Vision*, volume 1, pages 749–755, Beijing, China, October 2005. IEEE Computer Society Press.
- [4] A. Bruhn, J. Weickert, T. Kohlberger, and C. Schnörr. A multigrid platform for real-time motion computation with discontinuity-preserving variational methods. *International Journal of Computer Vision*, 70(3):257–277, December 2006.
- [5] C. Frohn-Schauf, S. Henn, and K. Witsch. Nonlinear multigrid methods for total variation denoising. *Computating and Visualization in Sciene*, 7(3–4):199–206, 2004.
- [6] B. Horn and B. Schunck. Determining optical flow. *Artificial Intelligence*, 17:185–203, 1981.
- [7] E. Mémin and P. Pérez. Dense estimation and object-based segmentation of the optical flow with robust techniques. *IEEE Transactions on Image Processing*, 7(5):703–719, May 1998.
- [8] N. Sundaram, T. Brox, and K. Keutzer. Dense point trajectories by GPU-accelerated large displacement optical flow. Technical Report UCB/EECS-2010-104, Department of Electrical Engineering and Computer Science, University of California, Berkeley, 2010.
- [9] L. Valgaerts, A. Bruhn, H. Zimmer, J. Weickert, C. Stoll, and C. Theobalt. Joint estimation of motion, structure and geometry from stereo sequences. In K. Daniilidis, P. Maragos, and N Paragios, editors, *Computer Vision – ECCV 2010*, volume 6314 of *Lecture Notes in Computer Science*, pages 568–581. Springer, Berlin, 2010.
- [10] H. Zimmer, A. Bruhn, and J. Weickert. Optic flow in harmony. *International Journal of Computer Vision*, 93(3):368–388, April 2011.